



ARTICLE

<https://doi.org/10.1038/s41467-019-08697-x>

OPEN

Oxygen vacancy associated single-electron transfer for photofixation of CO₂ to long-chain chemicals

Shichuan Chen¹, Hui Wang¹, Zhixiong Kang¹, Sen Jin¹, Xiaodong Zhang ¹, Xusheng Zheng², Zeming Qi², Junfa Zhu ², Bikai Pan¹ & Yi Xie¹

The photofixation and utilization of CO₂ via single-electron mechanism is considered to be a clean and green way to produce high-value-added commodity chemicals with long carbon chains. However, this topic has not been fully explored for the highly negative reduction potential in the formation of reactive carbonate radical. Herein, by taking Bi₂O₃ nanosheets as a model system, we illustrate that oxygen vacancies confined in atomic layers can lower the adsorption energy of CO₂ on the reactive sites, and thus activate CO₂ by single-electron transfer in mild conditions. As demonstrated, Bi₂O₃ nanosheets with rich oxygen vacancies show enhanced generation of •CO₂⁻ species during the reaction process and achieve a high conversion yield of dimethyl carbonate (DMC) with nearly 100% selectivity in the presence of methanol. This study establishes a practical way for the photofixation of CO₂ to long-chain chemicals via defect engineering.

¹Hefei National Laboratory for Physical Sciences at the Microscale, Collaborative Innovation Center of Chemistry for Energy Materials, University of Science and Technology of China, Hefei 230026, P.R. China. ²National Synchrotron Radiation Laboratory, University of Science and Technology of China, Hefei 230029, P.R. China. These authors contributed equally: Shichuan Chen, Hui Wang. Correspondence and requests for materials should be addressed to X.Z. (email: zhxid@ustc.edu.cn) Y.X. (email: yxie@ustc.edu.cn)

Continuous accumulation of carbon dioxide (CO₂) in the atmosphere represents a major contributor to climate change through global warming^{1,2}. In the past decades, the fixation and utilization of CO₂ has attracted great research interests all over the world, where the waste CO₂ could be converted to valuable chemicals for further use^{3–5}. In view of the strong carbon–oxygen bonds among the no electric dipole molecules, the conversion of inert CO₂ to other chemicals has been often performed under high temperature and pressure^{6–8}. Compared to traditional thermal based processes, light-driven CO₂ fixation may be a clean and cost-effective strategy to solve the energy issues and environmental problems^{9–13}.

Because of the highly negative reduction potential for the formation of reactive carbonate radical ($\bullet\text{CO}_2^-$, -1.9 V vs NHE), the photoreduction of CO₂ often undergoes a proton-assisted multi-electrons transfer process to overcome the high energies^{14,15}. However, the process is inaccessible for producing high-value-added organic chemicals with chains longer than three carbons, which could possess wide industrial applications and great economic value. For example, one of the most important long-chain chemicals, dimethyl carbonate (DMC), is a versatile and green chemical reagent, and has been widely used as fuel additive, electrolyte in lithium-ion batteries, monomer for organic synthesis, etc^{16–18}. Up to now, the synthetic routes of DMC or other long-chain chemicals often undergo high temperature and use of toxic and explosive agents, such as phosgene, hydrogen chloride, and carbon monoxide^{17,18}. Compared to traditional strategies, the photofixation of CO₂ to long-chain chemicals would be extremely attractive for its green and environmental friendly nature. In that case, it is essential for us to design the light harvesting semiconductors capable of activating CO₂ molecules with a single electron to the direct synthesis of long-chain chemicals, which is also the rate-determining step for CO₂ photofixation^{19,20}.

Bearing it in mind, we pay our attention to the catalysts with surface deficiency, where the introduced defects serve as reactive centers to adsorb gas molecules and hence activate them by lowering the adsorption energies. To go further, for the presence of abundant localized electrons in the defect sites, the enhanced charge transfer between catalysts and adsorbates could be realized. Thus, we propose that the atomically thin layers with rich surface defects and fully exposed active sites shall be an ideal structural model of pursuing high CO₂ photofixation efficiency.

Results

Theoretical studies. Herein, by taking the Bi₂O₃ atomic layers with oxygen vacancies (OVs) as an example, we studied the role of surface deficiency in CO₂ photoactivation, whose electronic structures and adsorption with CO₂ were investigated via density functional theory (DFT) calculations. As seen from the calculated density of states (DOS), the presence of OVs results in the appearance of a new defect level in Bi₂O₃ atomic layers, which is beneficial to the photoexcitation of electrons to the conduction band (Supplementary Fig. 1)^{21,22}. In addition, the differences of charge density between the Bi₂O₃ atomic layers and their defective structure (lower part of Fig. 1) clearly indicate that the electrons neighboring OVs could be localized, suggesting the electrons in the defect structures are more likely to be excited¹⁹. To go further, the CO₂ adsorption on the Bi₂O₃ atomic layers with and without OVs was performed to gain insights into the role of OVs in the chemisorption processes. As expected, the Bi₂O₃ atomic layers with OVs show promising CO₂ adsorption ability with negative adsorption energy of about -0.30 eV , while the chemisorption of CO₂ on the perfect Bi₂O₃ atomic layers was ruled out because of the weak interaction (Fig. 1). As shown in

the lower part of Fig. 1, the yellow and blue isosurfaces represent charge accumulation and depletion in the space, respectively, indicating the presence of exchange and transfer of electrons between the OVs and CO₂. Therefore, based on the above advantages, the Bi₂O₃ atomic layers with rich OVs would be efficient catalysts to overcome the bottlenecks of carbonate radical generation for CO₂ photofixation.

Synthesis and characterization. In this study, Bi₂O₃ atomic layers were prepared via in situ oxidation of freshly exfoliated Bi nanosheets owing to their high surface energy²³, during which oxygen deficiencies could be readily introduced (Fig. 2a). Meanwhile, the short in situ oxidation time benefits the generation of a high concentration of OVs. By taking the sample synthesized with 1 h oxidation as an example, the X-ray diffraction (XRD) pattern of its collected powers could be readily indexed to Bi₂O₃ (JCPDS Card No. 71–0465) with high phase purity (Supplementary Fig. 2). The Fourier-transform infrared (FT-IR) spectra show that the intercalated amine in the Bi-amine hybrid intermediate was simultaneously removed during the exfoliation and in situ oxidation processes (Supplementary Fig. 3), suggesting the clean surface of as-obtained sample²⁴. As shown in Fig. 2b of transmission electron microscopy (TEM) image, the synthetic sample shows a sheet-like morphology. In addition, atomic force microscopy (AFM) and corresponding height profiles of the nanosheets show an average thickness of 0.68 nm (Fig. 2c, d), which was consistent with the thickness of single-unit-cell Bi₂O₃ slab. The above results indicate that the Bi₂O₃ nanosheets with single-layer thickness were obtained.

To gain insights into the deficiencies in the as-prepared nanosheets, aberration-corrected high-angle annular dark-field scanning transmission electron microscopy (HAADF-STEM) was first carried out to show their fine structures. As displayed in Fig. 3a and Supplementary Fig. 4, the nanosheets show the interplanar spacings of 0.27 and 0.34 nm , corresponding to the distances of the (200) and (002) planes of Bi₂O₃, respectively, and indicating they are mostly enclosed by (010) faces. In addition, as compared to the sample with a long oxidation time of 6 h, the sample with short oxidation time shows obvious lattice disorder as labeled in Fig. 3a, which may be derived from the vacancies induced by the unsaturated coordination of metal atoms²⁵. To further explore their defect structure, X-ray photoelectron spectroscopy (XPS) was employed to study the valence states of the samples, where the O 2p peak located at 529.8 eV is attributed to the lattice oxygen, while the other one located at 530.9 eV is the signal of oxygen atoms in the vicinity of an OV^{25,26}. Notably, as clearly displayed in Fig. 3b, the sample with 1 h oxidation possesses more OVs than that with 6 h oxidation (Fig. 3b), which were labeled as oxygen vacancies-rich Bi₂O₃ nanosheet (OV-rich-Bi₂O₃) and oxygen vacancies-poor Bi₂O₃ nanosheet (OV-poor-Bi₂O₃), respectively. Furthermore, electron spin resonance (ESR) spectroscopy was performed to study the concentration of OVs in the samples. As shown in Fig. 3c, both the samples exhibited similar ESR signal ($g = 2.002$), which could be identified as the electrons trapped in OVs²⁵. OV-rich-Bi₂O₃ shows a greatly enhanced intensity in ESR signal than OV-poor-Bi₂O₃. It is known that, OVs could emit photoluminescence (PL) under light excitation, thus PL spectra were further performed to investigate the defects in the samples. As seen in Fig. 3d, both samples show two distinct PL emissions that could be ascribed to the signal of recombination of photogenerated electron–hole pairs (443 nm) and OVs (613 nm)²⁶, respectively. The PL emission intensity of OV-rich-Bi₂O₃ is lower than OV-poor-Bi₂O₃, which implies that OVs could hinder the recombination of photogenerated carriers in the Bi₂O₃ nanosheets⁵. And OV-rich-Bi₂O₃ possesses higher

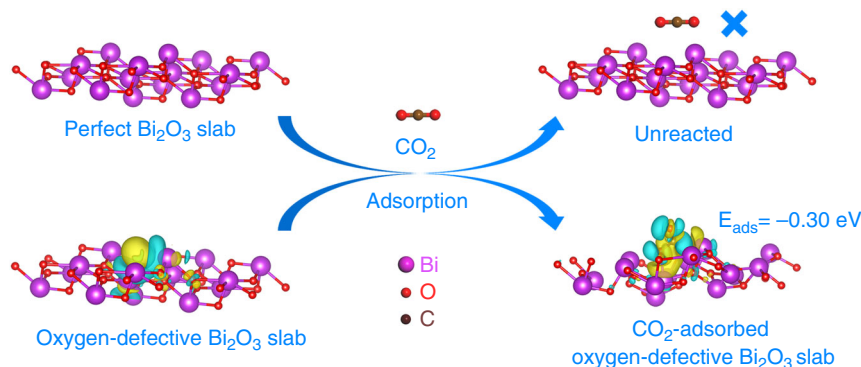


Fig. 1 Theoretical study. Schematic illustration of the adsorption of CO₂ molecules onto perfect and oxygen-defective Bi₂O₃ single-unit-cell layer slab with the partial charge density of oxygen vacancies

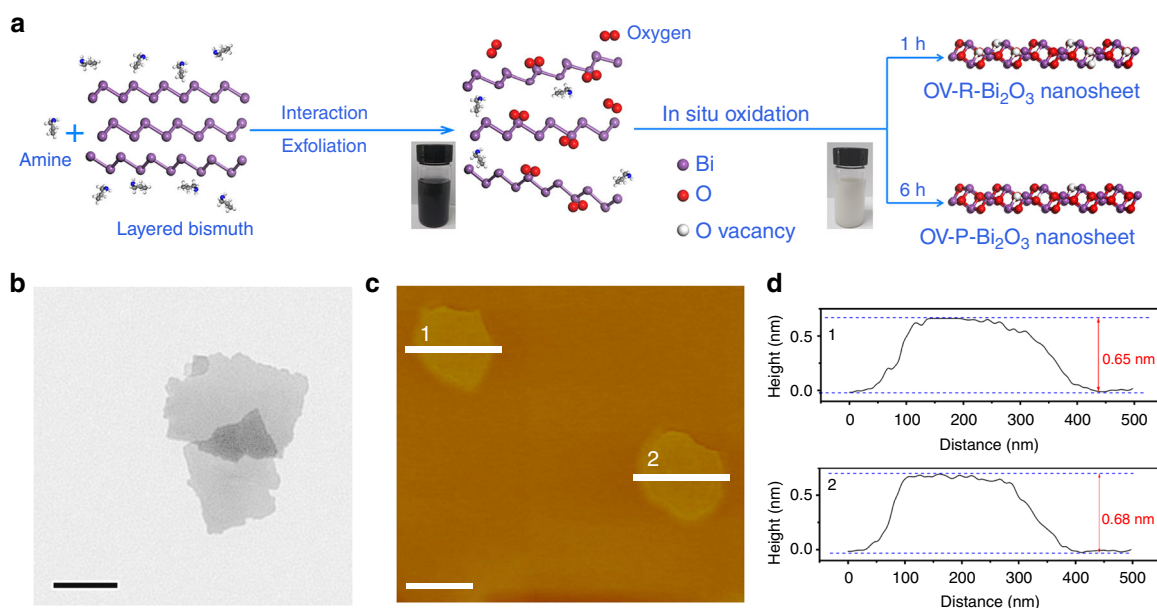


Fig. 2 Synthesis and morphology study. **a** Schematic introduction for the preparation of ultrathin Bi₂O₃ nanosheets with rich/poor oxygen vacancies. **b** TEM image of the OV-rich-Bi₂O₃ nanosheets. **c**, **d** AFM image and the height distributions (close to the regions of Line 1 and 2) of the OV-rich-Bi₂O₃ nanosheets, respectively. The scale bars in **(b, c)** are 200 nm

PL intensity of the peak 613 nm compared to OV-poor-Bi₂O₃, which is in agreement with the XPS and ESR analysis. Hence, the collective results shown above prove that OV-rich-Bi₂O₃ nanosheets with an abundant amount of OVs have been successfully designed.

Catalytic performances and mechanistic investigation. As known, the presence of OVs could strongly affect the adsorption of gas molecules and the catalytic activity of the catalysts. Herein, by taking the photofixation of CO₂ to high-value-added DMC in the presence of CH₃OH for an example, we systematically studied the catalytic ability of the Bi₂O₃ nanosheets with OVs. In situ diffuse reflectance infrared Fourier-transform spectroscopy (DRIFT) was carried out to investigate the local information for reaction species and their intermediates on the surface of the Bi₂O₃ nanosheets during the reaction^{27–30}. As shown in Fig. 4a, after treating the OV-rich-Bi₂O₃ nanosheets in the mixture of CO₂ and CH₃OH under light irradiation, three new peaks at 1294, 1456, and 1779 cm⁻¹ were generated, which could be assigned to the vibration of •CO₂⁻, carbonate-like (CO₃⁼) species and DMC, respectively^{27,29}. The intensities of the peaks gradually

increased with increasing reaction time. Meanwhile, as prolonging the reaction time to 60 min and the catalysis reaching a steady state, the reaction intermediate •CO₂⁻ is expected to level off while the final product DMC continues to rise (Fig. 4a). It is worth noting that, the formation of •CO₂⁻ species is the rate-determining step for the generation of DMC³¹. As expected, only OV-rich-Bi₂O₃ nanosheets could effectively activate CO₂ and initiate the reaction (Fig. 4b).

To further explore the intermediate states in the reaction, the adsorption ability of CO₂ in the surface of OV-rich-Bi₂O₃ was studied by quasi in situ XPS measurements under the simulated reaction conditions (CO₂ (0.2 MPa) at 373 K under Xe-lamp irradiation)^{32,33}. As shown in Fig. 4c of the C 1s spectra, besides the intrinsic peak of carbon bonds at 284.8 eV, there was a new peak located at about 288.3 eV, corresponding to the signal of •CO₂⁻ species^{34,35}. The experimental observations of •CO₂⁻ species indicates that the Bi₂O₃ nanosheets with OVs could be efficient catalysts for activating CO₂ via single-electron strategy. And it is anticipated that OV-rich-Bi₂O₃ show enhanced ability in the generation of •CO₂⁻ species compared to OV-poor-Bi₂O₃, corresponding well to the in situ DRIFT results. Based on the above observations, we can conclude that surface OVs in the

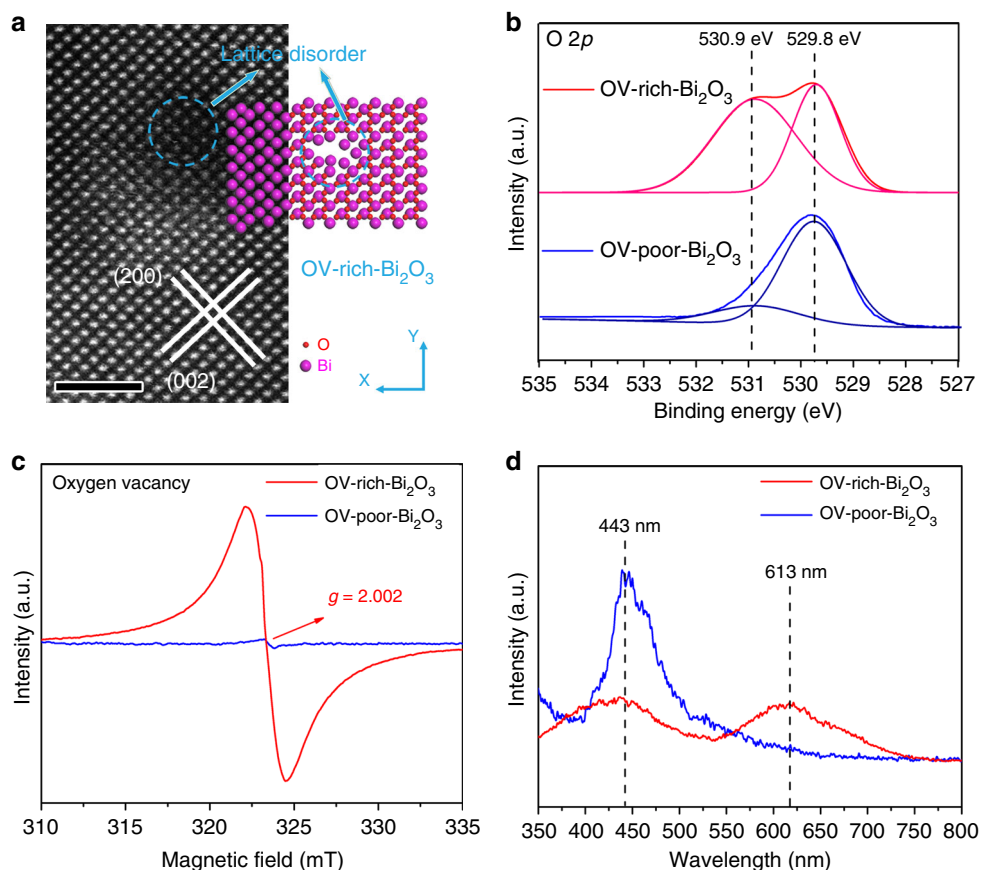


Fig. 3 Structure characterizations for the defect-controlled Bi_2O_3 nanosheets. **a** Atomic-resolution HAADF-STEM images and corresponding structure model of OV-rich- Bi_2O_3 nanosheets. The scale bar is 2 nm. **b** O 2p XPS spectra, **c** Room-temperature ESR spectra, and **d** PL spectra of Bi_2O_3 nanosheets with rich and poor oxygen vacancies, respectively

Bi_2O_3 nanosheets could enhance the formation of $\bullet\text{CO}_2^-$ species and carbonate-like (CO_3^-) species, which are the most important intermediate states in the reactions of CO_2 conversion. To further understand the reaction mechanism, ESR spectroscopy was carried out to detect and identify the generated radical species during the reaction by using 5,5-dimethyl-1-pyrroline N-oxide (DMPO) as a trapping reagent³⁶. As displayed in Supplementary Fig. 5, the methanol solution with Bi_2O_3 nanosheets gave rise to a six-line spectrum, which can be attributed to the DMPO- CH_3 adducts, and thus it is reasonable to infer the generation of $\bullet\text{CH}_3$ intermediate in the reaction processes.

Based on the above analysis, the direct photogeneration of DMC from the reaction of CO_2 and CH_3OH was conducted in acetonitrile (CH_3CN) solution with CO_2 pressure of 0.2 MPa at 373 K (the products were detected by nuclear magnetic resonance (NMR) spectroscopy, Supplementary Fig. 6). As shown in Fig. 5a and Supplementary Table 1, both OV-rich- Bi_2O_3 and OV-poor- Bi_2O_3 nanosheets could catalyze CO_2 and CH_3OH to DMC with nearly 100% selectivity, despite trace amounts of DMC can be detected in the presence of bulk Bi_2O_3 , being consistent with the result of Fig. 4b. Meanwhile, the conversion yield of OV-rich- Bi_2O_3 can reach to about 18%, which is 9 times higher than that of OV-poor- Bi_2O_3 , indicating the OVs in Bi_2O_3 nanosheets offer indispensable active sites for the reactions. The $^{13}\text{CO}_2$ labeling experiment is a useful tool to reveal the dominant product indeed originated from the photofixation of CO_2 or not. The isotope tracing experiments were performed using common CO_2 and $^{13}\text{CO}_2$ (^{13}C , 99%), respectively. The $^{13}\text{CO}_2$ labelling experiments involving the same set-up and reaction condition

both yielded a product that generates an obvious ^{13}C NMR peaks at 156.6-ppm and 54.8-ppm signals referring to DMC (Supplementary Fig. 6b)³⁷. The labelling carbon at 156.6-ppm comes from carbon sources CO_2 and another labelling carbon at 54.8-ppm comes from CH_3OH . In the experiment, we employed the $^{13}\text{CO}_2$ as ^{13}C -labeled carbon sources. The intensity of $^{13}\text{CO}_2$ that located at 156.6-ppm is much higher than that of common CO_2 , thus clearly indicating that the product DMC is indeed derived from CO_2 . The nearly identical BET surface area as displayed in Supplementary Fig. 7 further implied the crucial role of OVs in the catalytic performance of the Bi_2O_3 atomic layers. It is worth noting that, the high conversion yield and nearly 100% selectivity of OV-rich- Bi_2O_3 nanosheets under mild conditions are superior to most of previously reported catalysts, which were commonly conducted in high temperature and pressure (Supplementary Table 1). In order to further show the catalytic performances of our samples, we have compared OV-rich- Bi_2O_3 nanosheets with other well-established catalysts under the same reaction conditions, including CeO_2 nanosheets, V_2O_5 nanosheets and ZrO_2 nanoparticles^{38–40}. As seen in the Supplementary Fig. 8, the conversion yield of OV-rich- Bi_2O_3 nanosheets was much higher than that of the other three catalysts, indicating the outstanding catalytic performances of OV-rich- Bi_2O_3 nanosheets for DMC generation. Moreover, OV-rich- Bi_2O_3 nanosheets exhibited high stability after 25 catalytic cycles up to 200 h in Fig. 5b, during which their morphology and defective structure were also retained (Supplementary Fig. 9). Thus, OV-rich- Bi_2O_3 nanosheets were efficient catalysts for photocatalytic DMC production.

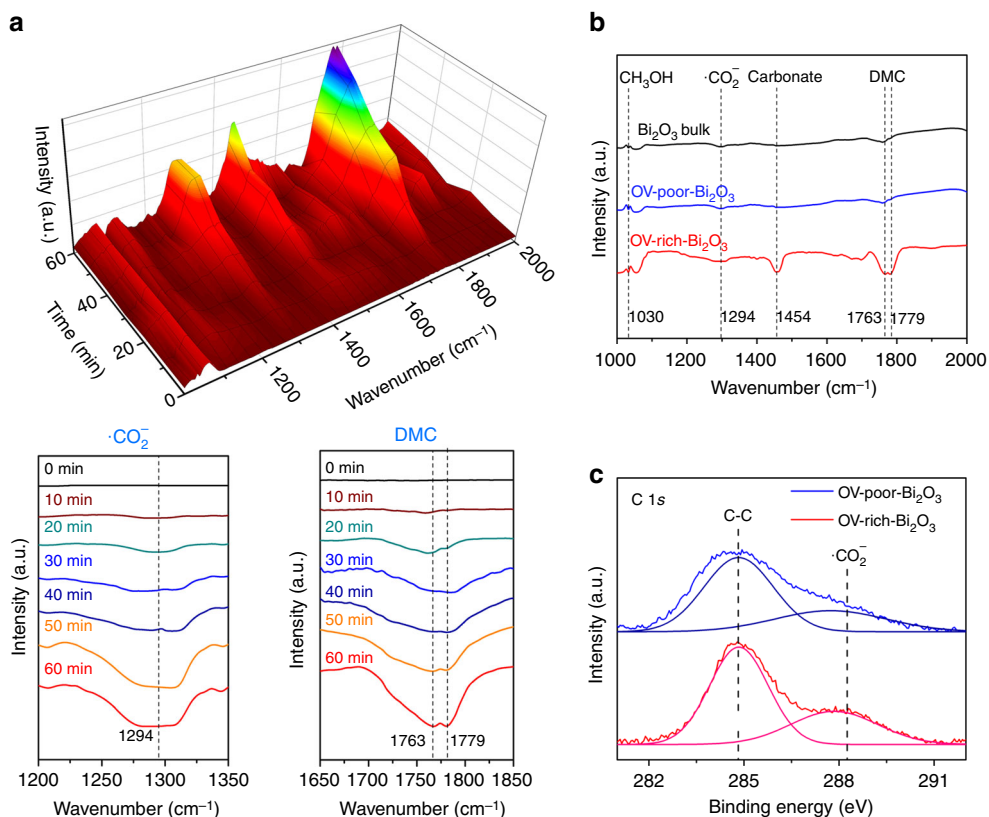


Fig. 4 Reaction mechanism for Bi₂O₃ nanosheets. **a** In situ DRIFTS spectra for the adsorption and activation of CO₂ in the presence of CH₃OH under Xe-lamp irradiation for OV-rich-Bi₂O₃ nanosheets. Inset at the lower left: the DRIFTS of generation of $\cdot\text{CO}_2^-$; inset at the lower right: the DRIFTS of DMC. **b** In situ DRIFTS spectra for the catalysts with CO₂ and CH₃OH under Xe-lamp irradiation for 60 min. **c** Quasi in situ XPS spectra of OV-rich-Bi₂O₃ and OV-poor-Bi₂O₃ nanosheets under the atmosphere of CO₂ (0.2 MPa) at 373 K

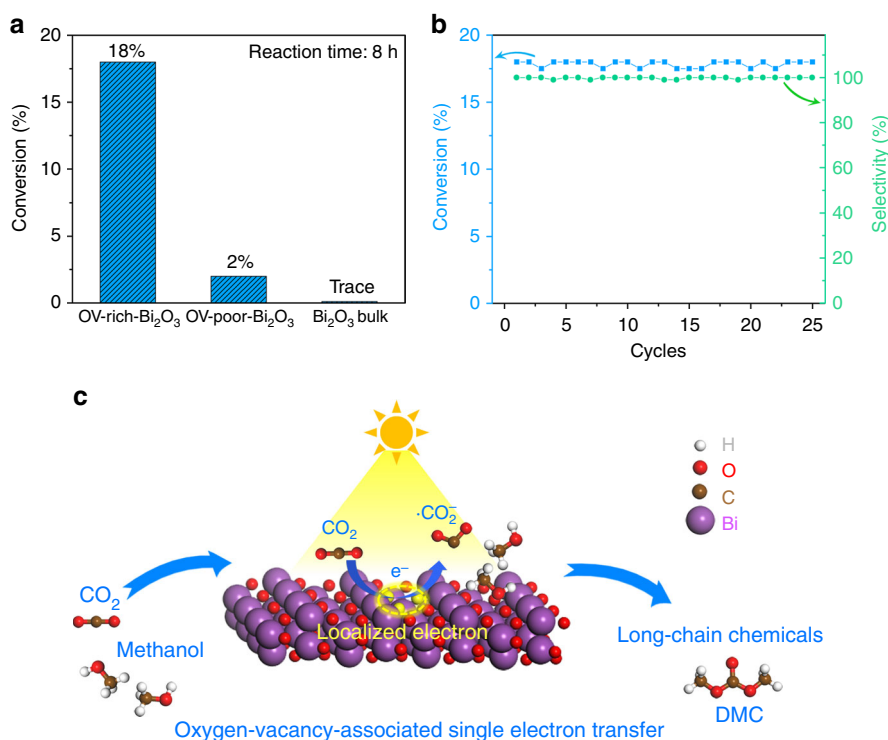
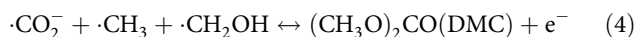
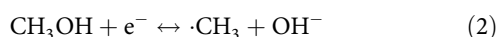
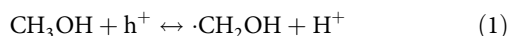


Fig. 5 Catalytic performances and schematic reaction processes. **a** Performances of various catalysts for CO₂ fixation at 373 K under Xe-lamp irradiation. **b** Photostability cyclic test for OV-rich-Bi₂O₃ nanosheets. Reaction time for each run: 8 h. **c** Schematic introduction for the photofixation of CO₂ to long-chain chemicals

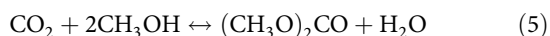
As one of the key factors for photocatalysis, the band structures of the synthetic Bi₂O₃ nanosheets were tested to explore the role of OV in achieving high activity in photoreduction of CO₂. Based on the analysis of Mott-Schottky curves, UV-vis spectra and synchrotron radiation photoelectron spectroscopy (SRPES), the conduction band minimum (CBMs) of OV-rich-Bi₂O₃ nanosheets and OV-poor-Bi₂O₃ nanosheets were determined to be -0.11 eV and -0.08 eV (vs. normal hydrogen electrode (NHE)), respectively (Supplementary Fig. 10). Interestingly, although the conduction band position of the synthetic Bi₂O₃ nanosheets is well below the reduction level for carbonate radical (CO₂ + e⁻ → •CO₂⁻, E⁰ = -1.9 V vs. NHE), the nanosheets could still break the thermodynamic limitations of CO₂ activation, further confirming the crucial role of OV in activating of CO₂ on the surface of Bi₂O₃ nanosheets.

Discussion

Based on the combination of theoretical and experimental studies, the reaction for the photofixation of CO₂ with methanol to DMC involves four consequently elementary steps described as followings, among which the generation of •CO₂⁻ group is the rate-limiting step^{9,20,31}.



Summary:



As schematically illustrated in Fig. 5c, the OVs confined in Bi₂O₃ nanosheets serve as the efficiently active sites for the adsorption and activation of CO₂ to •CO₂⁻. In detail, the OVs in the surface of Bi₂O₃ nanosheets offer abundant coordinatively unsaturated sites for the adsorption of CO₂ molecules^{25,31}. Meanwhile, the electrons that localized on the OVs are easily to be excited for CO₂ activation. In addition, rich OVs could result in the enhanced separation of photogenerated electron and holes in the samples to offer abundant free charge carriers, as illustrated in the photocurrent-voltage curves (Supplementary Fig. 11). Furthermore, CH₃OH molecules intended to be adsorbed on the nanosheets with OVs, exhibiting more negative adsorption energy compared to its vacancy-free counterpart^{41,42}. Benefitting from the above advantages, the efficient reduction of CO₂ to long-chain chemicals at the OVs in the Bi₂O₃ nanosheets could be realized.

In conclusion, we have shown that Bi₂O₃ nanosheets with rich OVs are efficient catalysts for the photofixation of CO₂ to valuable long-chain chemicals. Theoretical simulations showed that the OVs can not only provide abundant localized electrons, but also lower the adsorption energies of CO₂ on the Bi₂O₃ atomic layers. Both in situ DRIFT and quasi in situ XPS reveal that OVs in the Bi₂O₃ nanosheets could enhance the generation of •CO₂⁻ species, which is the rate-determining step for CO₂ photofixation. As a result, the OV-rich-Bi₂O₃ nanosheets could catalyze CO₂ and CH₃OH to DMC with extremely high selectivity, whereas only trace amounts of DMC can be detected for pristine bulk Bi₂O₃. This work not only paves the way to the design of efficient catalysts for the synthesis of long-chain chemicals, but also

provides insights into the role of defective structures in the CO₂ photofixation process.

Methods

Materials. Bismuth powders were purchased from Aladdin. Citric acid (CA, >99.5%) and 5,5-dimethyl-1-pyrroline N-oxide (DMPO, for ESR tests) were purchased from Sigma-Aldrich. D(+)-Glucose (AR), hydrochloric acid (36~38%, AR), anhydrous ethanol (EtOH, AR), ethyl acetate (EtOAc, AR) and acetonitrile (CH₃CN, AR) were obtained from Sinopharm Chemical Reagent Co., Ltd. The water used in all experiments was de-ionized (DI). Other chemicals were of analytical grade purity, obtained from Sinopharm Chemical Reagent Co., Ltd. All of the chemical reagents of analytical grade were used as received without further purification.

Preparation of Oxygen-vacancy-controlled Bi₂O₃ nanosheets. In a typical synthesis, 800 mg Bismuth (Alfa Aesar) was added into a mixed solution of benzyl alcohol (30 mL) and propylamine (6 mL). After vigorous stirring for 20 min, the mixture was then transferred into a 50 ml Teflon-lined autoclave, sealed and heated at 453 K for 12 h. The system was then allowed to cool down to room temperature naturally; the precipitates were collected by centrifugation, washed with ethanol and water for many times then dried in vacuum overnight for further use. Then, 400 mg the following the precipitates was dispersed into 100 ml mixed solution of isopropanol and water (1:1) that bubbled with oxygen to induce the oxidation of bismuth, and the mixture solution was then sonicated at the power of 300 W. The oxygen vacancy-rich ultrathin Bi₂O₃ nanosheets (OV-rich-Bi₂O₃) were formed by ultrasounding for 1 h. The oxygen vacancy-poor ultrathin Bi₂O₃ nanosheets (OV-poor-Bi₂O₃) were obtained by ultrasounding for 6 h.

Preparation of bulk Bi₂O₃. In a typical synthesis, 2 mmol Na₂SO₄ and 4 mmol Bi(NO₃)₃·5H₂O was dissolved in 30 ml deionized water. Then the pH values of the mixture were adjusted to 11 by adding of 1 M NaOH solution. The mixture was then transferred into a 50 ml Teflon-lined autoclave, sealed and heated at 473 K for 12 h. The system was then allowed to cool down to room temperature naturally; the precipitates were collected by centrifugation, washed with ethanol and water for several times, and then dried in vacuum overnight for further use.

Characterizations. XRD spectra was collected by Philips X'Pert Pro Super diffractometer with Cu-Kα radiation (λ = 1.54178 Å). The HAADF-STEM measurement was carried out on a JEOL JEM-ARF200F. The ESR measurements were recorded on a JES-FA200 model spectrometer operating at the X-band frequency. AFM was measured on the Veeco DI Nano-scope MultiMode V system. The X-ray photoelectron spectra (XPS) were detected on an ESCALAB MKII with Mg Kα as the excitation source, using C 1s (284.6 eV) as a reference. The Fourier-transform infrared (FT-IR) spectra were collected on a MAGNA-IR 750 (Nicolet Instrument Co., U.S.). Room temperature PL spectra were carried out by using a Jobin Yvon Fluorolog 32TAU luminescence spectrometer (Jobin Yvon Instruments Co., Ltd., France). The valence band XPS spectra were detected at beamline BL10B in the National Synchrotron Radiation Laboratory (NSRL), Hefei, China. The NMR experiments were carried out on with a 400-MHz Bruker AVANCE AV III NMR spectrometer. The electrochemical measurements were performed an electrochemical workstation (CHI760E, Shanghai Chenhua Limited, China). Isotope Tracing Experiments: The isotope tracing experiments were performed using ¹³CO₂ (99%, Cambridge Isotope Laboratories, Inc.) and the corresponding products were measured by determined via the ¹³C-coupled satellites in a 400-MHz Bruker AVANCE AV III NMR spectrometer.

Calculation method. The first-principles DFT calculations were carried out with the projected augmented wave method with the Perdew-Burke-Ernzerhof (PBE) GGA functional encoded in the Vienna ab initio simulation package⁴³. The convergence on the choice of energy cut-off was tested to 400 eV, and the atomic positions were allowed to relax until the energy and force are <10⁻⁴ eV and -0.02 eV Å⁻¹, respectively.

Catalytic tests. The direct photogeneration of DMC was performed from the reaction of CO₂ and CH₃OH in a 100 mL stainless-steel autoclave. After the addition of 30 mL of acetonitrile (CH₃CN) solution and 20 mg catalysts into a Teflon inlet, the autoclave was pressurized with high-purity CO₂ pressure (99.99%, 0.2 MPa). The reaction was performed at 373 K with stirring at 400 r.p.m. for 8 h. The light source for the photocatalysis was a 300 W Xe lamp (PLS-SXE300/300UV, Beijing Perfectlight Technology Co., Ltd). The liquid products were detected by NMR (400-MHz Bruker AVANCE AV III) spectroscopy using 1,4-dicyanobenzene as the internal standard.

In situ DRIFTS measurements. In situ diffuse reflectance infrared Fourier-transform spectroscopy (DRIFTS) measurements were obtained by using a Bruker IFS 66v Fourier-transform spectrometer equipped with a Harrick diffuse reflectance accessory at the Infrared Spectroscopy and Microspectroscopy Endstation (BL01B) in

NSRL in Hefei, China. The samples were held in a custom-fabricated IR reaction chamber which was specifically designed to examine highly scattering powder samples in the diffuse reflection mode. The chamber was sealed with two ZnSe windows. During the in situ characterization, 0.2 MPa of CO₂ was introduced into the chamber and the peaks of free molecular CO₂ were set as a reference between the samples. Each spectrum was recorded by averaging 256 scans at a 4 cm⁻¹ spectral resolution.

Quasi in situ XPS measurements. The quasi in situ XPS measurements were performed at the photoemission end-station at beamline BL10B in the NSRL in Hefei, China. Briefly, the beamline is connected to a bending magnet and covers photon energies from 100 to 1000 eV with a resolving power ($E/\Delta E$) better than 1000. The end-station is composed of four chambers, i.e., analysis chamber, preparation chamber, quick sample load-lock chamber and high pressure reactor. The analysis chamber, with a base pressure of $<5 \times 10^{-10}$ torr, is connected to the beamline and equipped with a VG Scienta R3000 electron energy analyzer and a twin anode X-ray source. After the sample treatment, the reactor can be pumped down to high vacuum ($<10^{-8}$ torr) for sample transfer. In the current work, the samples were treated with the CO₂ (0.2 Mpa) at 373 K for 2 h under Xe-lamp irradiation, after which it was transferred to analysis chamber for XPS measurement without exposing to air.

Data availability

The data that support the findings of this study are available on request from the corresponding authors.

Received: 26 July 2018 Accepted: 20 January 2019

Published online: 15 February 2019

References

- Lin, S. et al. Covalent organic frameworks comprising cobalt porphyrins for catalytic CO₂ reduction in water. *Science* **349**, 1208–1213 (2015).
- Cao, Z. et al. A molecular surface functionalization approach to tuning nanoparticle electrocatalysts for carbon dioxide reduction. *J. Am. Chem. Soc.* **138**, 8120–8125 (2016).
- Gao, S. et al. Partially oxidized atomic cobalt layers for carbon dioxide electroreduction to liquid fuel. *Nature* **529**, 68–71 (2016).
- Kim, D., Resasco, J., Yu, Y., Asiri, A. M. & Yang, P. Synergistic geometric and electronic effects for electrochemical reduction of carbon dioxide using gold-copper bimetallic nanoparticles. *Nat. Commun.* **5**, 4948 (2014).
- Yang, H. B. et al. Atomically dispersed Ni(i) as the active site for electrochemical CO₂ reduction. *Nat. Energy* **3**, 140–147 (2018).
- Stoian, D. C. et al. Boosted CO₂ reaction with methanol to yield dimethyl carbonate over Mg-Al hydrotalcite-silica lyogels. *Chem. Commun.* **49**, 5489–5491 (2013).
- Bian, J. et al. Highly effective synthesis of dimethyl carbonate from methanol and carbon dioxide using a novel copper–nickel/graphite bimetallic nanocomposite catalyst. *Chem. Eng. J.* **147**, 287–296 (2009).
- Wu, X. L., Meng, Y. Z., Xiao, M. & Lu, Y. X. Direct synthesis of dimethyl carbonate (DMC) using Cu–Ni/VSO as catalyst. *J. Mol. Catal. A: Chem.* **249**, 93–97 (2006).
- Maeda, K. et al. Photocatalyst releasing hydrogen from water. *Nature* **440**, 295 (2006).
- Bachmeier, A., Hall, S., Ragsdale, S. W. & Armstrong, F. A. Selective visible-light-driven CO₂ reduction on a p-type dye-sensitized NiO photocathode. *J. Am. Chem. Soc.* **136**, 13518–13521 (2014).
- Meng, X. et al. Photothermal conversion of CO₂ into CH₄ with H₂ over Group VIII nanocatalysts: an alternative approach for solar fuel production. *Angew. Chem. Int. Ed.* **53**, 11478–11482 (2014).
- Rao, H., Schmidt, L. C., Bonin, J. & Robert, M. Visible-light-driven methane formation from CO₂ with a molecular iron catalyst. *Nature* **548**, 74–77 (2017).
- Schreier, M. et al. Solar conversion of CO₂ to CO using Earth-abundant electrocatalysts prepared by atomic layer modification of CuO. *Nat. Energy* **2**, 17087 (2017).
- Benson, E. E., Kubiak, C. P., Sathrum, A. J. & Smieja, J. M. Electrocatalytic and homogeneous approaches to conversion of CO₂ to liquid fuels. *Chem. Soc. Rev.* **38**, 89–99 (2009).
- Halmann, M. Photoelectrochemical reduction of aqueous carbon dioxide on p-type gallium phosphide in liquid junction solar cells. *Nature* **275**, 115–116 (1978).
- Wang, J.-Q. et al. Synthesis of dimethyl carbonate from CO₂ and ethylene oxide catalyzed by K₂CO₃-based binary salts in the presence of H₂O. *Green. Chem.* **13**, 3213 (2011).
- Meylan, F. D., Moreau, V. & Erkman, S. CO₂ utilization in the perspective of industrial ecology, an overview. *J. CO₂Util.* **12**, 101–108 (2015).
- Eta, V. et al. Synthesis of dimethyl carbonate from methanol and carbon dioxide: circumventing thermodynamic limitations. *Ind. Eng. Chem. Res.* **49**, 9609–9617 (2010).
- Liu, L., Zhao, C. & Li, Y. Spontaneous dissociation of CO₂ to CO on defective surface of Cu(I)/TiO_{2-x} nanoparticles at room temperature. *J. Phys. Chem. C.* **116**, 7904–7912 (2012).
- Li, H., Shang, J., Ai, Z. & Zhang, L. Efficient visible light nitrogen fixation with BiOBr nanosheets of oxygen vacancies on the exposed {001} facets. *J. Am. Chem. Soc.* **137**, 6393–6399 (2015).
- Zhang, X. & Xie, Y. Recent advances in free-standing two-dimensional crystals with atomic thickness: design, assembly and transfer strategies. *Chem. Soc. Rev.* **42**, 8187–8199 (2013).
- Li, J., Zhan, G., Yu, Y. & Zhang, L. Superior visible light hydrogen evolution of Janus bilayer junctions via atomic-level charge flow steering. *Nat. Commun.* **7**, 11480 (2016).
- Su, C., Liu, H.-T. & Li, J.-M. Bismuth nanotubes: potential semiconducting nanomaterials. *Nanotechnology* **13**, 746–749 (2002).
- Sun, Y., Wang, W., Zhang, L. & Zhang, Z. Design and controllable synthesis of α - γ -Bi₂O₃ homojunction with synergetic effect on photocatalytic activity. *Chem. Eng. J.* **211–212**, 161–167 (2012).
- Zhang, N. et al. Oxide defect engineering enables to couple solar energy into oxygen activation. *J. Am. Chem. Soc.* **138**, 8928–8935 (2016).
- Wang, H. et al. Oxygen-vacancy-mediated exciton dissociation in BiOBr for boosting charge-carrier-involved molecular oxygen activation. *J. Am. Chem. Soc.* **140**, 1760–1766 (2018).
- Long, R. et al. Isolation of Cu atoms in Pd lattice: forming highly selective sites for photocatalytic conversion of CO₂ to CH₄. *J. Am. Chem. Soc.* **139**, 4486–4492 (2017).
- Wang, L. et al. Atomic-level insights in optimizing reaction paths for hydroformylation reaction over Rh/CoO single-atom catalyst. *Nat. Commun.* **7**, 14036 (2016).
- Neatu, S., Macia-Agullo, J. A., Concepcion, P. & Garcia, H. Gold-copper nanoalloys supported on TiO₂ as photocatalysts for CO reduction by water. *J. Am. Chem. Soc.* **136**, 15969–15976 (2014).
- Wang, L. et al. Incorporating nitrogen atoms into cobalt nanosheets as a strategy to boost catalytic activity toward CO₂ hydrogenation. *Nat. Energy* **2**, 869 (2017).
- Lee, J., Soreescu, D. C. & Deng, X. Electron-induced dissociation of CO₂ on TiO₂(110). *J. Am. Chem. Soc.* **133**, 10066–10069 (2011).
- Heine, C., Lechner, B. A., Bluhm, H. & Salmeron, M. Recycling of CO₂: probing the chemical state of the Ni(111) surface during the methanation reaction with ambient-pressure X-ray photoelectron spectroscopy. *J. Am. Chem. Soc.* **138**, 13246–13252 (2016).
- Wang, Y. et al. CO₂ photoreduction with H₂O vapor on highly dispersed CeO₂/TiO₂ catalysts: Surface species and their reactivity. *J. Catal.* **337**, 293–302 (2016).
- Ilegbusi, O. J. & Trakhtenberg, L. Synthesis and conductometric property of sol-gel-derived ZnO/PVP nano hybrid films. *J. Mater. Eng. Perform.* **22**, 911–915 (2012).
- Zhang, J.-Y., Esrom, H., Kogelschatz, U. & Emig, G. Modification of polymers with UV excimer radiation from lasers and lamps. *J. Adhes. Sci. Technol.* **8**, 1179–1210 (1994).
- Togashi, H. et al. Analysis of hepatic oxidative stress status by electron spin resonance spectroscopy and imaging. *Free. Radic. BiO. Med.* **28**, 846–853 (2000).
- Fulmer, G. R. et al. NMR chemical shifts of trace impurities: common laboratory solvents, organics, and gases in deuterated solvents relevant to the organometallic chemist. *Organometallics* **29**, 2176–2179 (2010).
- Sun, Y. et al. Pits confined in ultrathin cerium(IV) oxide for studying catalytic centers in carbon monoxide oxidation. *Nat. Commun.* **4**, 2899 (2013).
- Peng, X. et al. Hydrogenated V₂O₅ nanosheets for superior lithium storage properties. *Adv. Funct. Mater.* **26**, 784–791 (2016).
- Fakhri, A., Behrouz, S., Tyagi, I., Agarwal, S. & Gupta, V. K. Synthesis and characterization of ZrO₂ and carbon-doped ZrO₂ nanoparticles for photocatalytic application. *J. Mol. Liq.* **216**, 342–346 (2016).
- Wu, G.-S. et al. Implication of the role of oxygen anions and oxygen vacancies for methanol decomposition over zirconia supported copper catalysts. *Appl. Surf. Sci.* **253**, 974–982 (2006).
- de Armas, R. S., Oviedo, J., San Miguel, M. A. & Sanz, J. F. Methanol adsorption and dissociation on TiO₂(110) from first principles calculations. *J. Phys. Chem. C.* **111**, 10023–10028 (2007).
- Kresse, G. & Joubert, D. From ultrasoft pseudopotentials to the projector augmented-wave method. *Phys. Rev. B* **59**, 1758–1775 (1999).

Acknowledgements

This work was supported by the National Key R & D Program on Nano Science & Technology (2017YFA0207301), National Natural Science Foundation of China (U1632149, U1532265, 11621063, 21890754), Anhui Provincial Natural Science

Foundation (1708085QB24, 1808085QB34), the Youth Innovation Promotion Association of CAS (2017493), Young Elite Scientist Sponsorship Program by CAST, and Key Research Program of Frontier Sciences (QYZDY-SSW-SLH011). The authors thank Dr. Yang Xu at Ilmenau University of Technology for useful discussions.

Author contributions

X.D.Z. and Y.X. supervised the project. X.D.Z., S.C., and H.W. conceived the idea and wrote the paper. S.C., H.W. and S.J. carried the experiments and analyzed the results. Z. K. and B.P. performed the DFT calculations. X.S.Z., Z.Q. and J.Z. collected the synchrotron radiation based spectroscopy data. All authors discussed the results and assisted during manuscript preparation.

Additional information

Supplementary Information accompanies this paper at <https://doi.org/10.1038/s41467-019-08697-x>.

Competing interests: The authors declare no competing interests.

Reprints and permission information is available online at <http://npg.nature.com/reprintsandpermissions/>

Journal peer review information: *Nature Communications* thanks Zhongfang Chen and the other anonymous reviewer(s) for their contribution to the peer review of this work. Peer reviewer reports are available.

Publisher's note: Springer Nature remains neutral with regard to jurisdictional claims in published maps and institutional affiliations.



Open Access This article is licensed under a Creative Commons Attribution 4.0 International License, which permits use, sharing, adaptation, distribution and reproduction in any medium or format, as long as you give appropriate credit to the original author(s) and the source, provide a link to the Creative Commons license, and indicate if changes were made. The images or other third party material in this article are included in the article's Creative Commons license, unless indicated otherwise in a credit line to the material. If material is not included in the article's Creative Commons license and your intended use is not permitted by statutory regulation or exceeds the permitted use, you will need to obtain permission directly from the copyright holder. To view a copy of this license, visit <http://creativecommons.org/licenses/by/4.0/>.

© The Author(s) 2019